

**Manuscript version: Author's Accepted Manuscript**

The version presented in WRAP is the author's accepted manuscript and may differ from the published version or Version of Record.

**Persistent WRAP URL:**

<http://wrap.warwick.ac.uk/136237>

**How to cite:**

Please refer to published version for the most recent bibliographic citation information. If a published version is known of, the repository item page linked to above, will contain details on accessing it.

**Copyright and reuse:**

The Warwick Research Archive Portal (WRAP) makes this work by researchers of the University of Warwick available open access under the following conditions.

Copyright © and all moral rights to the version of the paper presented here belong to the individual author(s) and/or other copyright owners. To the extent reasonable and practicable the material made available in WRAP has been checked for eligibility before being made available.

Copies of full items can be used for personal research or study, educational, or not-for-profit purposes without prior permission or charge. Provided that the authors, title and full bibliographic details are credited, a hyperlink and/or URL is given for the original metadata page and the content is not changed in any way.

**Publisher's statement:**

Please refer to the repository item page, publisher's statement section, for further information.

For more information, please contact the WRAP Team at: [wrap@warwick.ac.uk](mailto:wrap@warwick.ac.uk).

# Ultrafast optoelectronic processes in 1D radial van der Waals heterostructures: carbon, boron nitride and MoS<sub>2</sub> nanotubes with coexisting excitons and highly mobile charges

Maria G. Burdanova,<sup>†</sup> Reza J. Kashtiban,<sup>†</sup> Yongjia Zheng,<sup>‡</sup> Rong Xiang,<sup>‡</sup>  
Shohei Chiashi,<sup>‡</sup> Jack Matthew Woolley,<sup>¶</sup> Michael Staniforth,<sup>¶</sup> Emily  
Sakamoto-Rablah,<sup>†</sup> Xue Xie,<sup>†</sup> Matthew Broome,<sup>†</sup> Jeremy Sloan,<sup>†</sup> Anton  
Anisimov,<sup>§</sup> Esko I. Kauppinen,<sup>||</sup> Shigeo Maruyama,<sup>‡</sup> and James Lloyd-Hughes<sup>\*,†</sup>

<sup>†</sup>*University of Warwick, Department of Physics, Gibbet Hill Road, Coventry, CV4 7AL,  
United Kingdom.*

<sup>‡</sup>*Department of Mechanical Engineering, The University of Tokyo, Tokyo 113-8656, Japan.*

<sup>¶</sup>*University of Warwick, Department of Chemistry, Gibbet Hill Road, Coventry, CV4 7AL,  
United Kingdom.*

<sup>§</sup>*Canatu Ltd., Helsinki FI00390, Finland.*

<sup>||</sup>*Department of Applied Physics, Aalto University School of Science, Espoo 15100,  
FI-00076 Aalto, Finland.*

E-mail: j.lloyd-hughes@warwick.ac.uk

## Abstract

Heterostructures built from 2D, atomically-thin crystals are bound by the van der Waals force, and exhibit unique optoelectronic properties. Here, we report the struc-

ture, composition and optoelectronic properties of 1D van der Waals heterostructures comprising carbon nanotubes wrapped by atomically-thin nanotubes of boron nitride and molybdenum disulfide ( $\text{MoS}_2$ ). The high quality of the composite was directly evidenced on the atomic scale by transmission electron microscopy, and on the macroscopic scale by a study of the heterostructure’s equilibrium and ultrafast optoelectronics. Ultrafast pump-probe spectroscopy across the visible and terahertz frequency ranges identified that, in the  $\text{MoS}_2$  nanotubes, excitons coexisted with a prominent population of free charges. The electron mobility was comparable to that found in high-quality atomically-thin crystals. The high mobility of the  $\text{MoS}_2$  nanotubes highlights the potential of 1D van der Waals heterostructures for nanoscale optoelectronic devices.

## Keywords

**nanotubes; van der Waals heterostructures; ultrafast; terahertz**

Atomically-thin crystals and their heterostructures are creating entirely new paradigms in the design of advanced optoelectronic materials. Novel 2D materials, as exemplified by the transition metal dichalcogenides (TMDs), feature exotic properties such as strong Coulomb interactions, efficient luminescence and spin-valley physics.<sup>1–5</sup> Significant exciton binding energies  $E_B$  arise from the weak, non-local dielectric screening of the Coulomb interaction in 2D atomically-thin TMDs, combined with the relatively high effective masses of carriers:<sup>5</sup> for instance  $E_B = 0.24 - 0.27$  eV for the A exciton in a  $\text{MoS}_2$  monolayer.<sup>6,7</sup>

Heterostructures of atomically-thin 2D materials show unique emergent properties associated with interlayer coupling and charge transfer, opening up new possibilities for the development of nanoelectronic devices.<sup>8,9</sup> In such van der Waals heterostructures, excitons can remain tightly bound even across lateral and vertical heterojunctions. While the study of 2D heterostructures has undergone rapid growth, 1D heterostructures<sup>10</sup> in a wire geometry offer unique nano-optoelectronic applications including field effect transistors, where inner carbon

nanotubes (CNTs) are used to electrically gate an outer TMD nanotube, such as  $\text{MoS}_2$ ,<sup>10</sup> or radial p-n junctions for nano-scale photovoltaics or photodetectors,<sup>11</sup> for instance exploiting flexoelectricity.<sup>12</sup> When 2D materials roll up to form 1D nanotubes, dramatic changes in the optoelectronic properties result from curvature and quantum confinement, as exemplified by the comparison between graphene, a Dirac semi-metal with no excitons, and semiconducting carbon nanotubes, which host excitons. Hence it is of fundamental and applied interest to explore the nature of quasiparticles created after photoexcitation of 1D TMDs.

Here we report the equilibrium and dynamic optoelectronic properties of a 1D van der Waals (vdW) heterostructure consisting of bundles of carbon nanotubes wrapped by boron nitride nanotubes (BNNTs) and molybdenum disulphide nanotubes ( $\text{MoS}_2$  NTs). Chemical vapour deposition created radial heterostructures, using free-standing films of carbon nanotubes as the initial template.<sup>10</sup> The BN overgrowth served to wrap each CNT bundle, creating a template with sufficient diameter ( $>5\text{ nm}$ ) for the subsequent deposition of atomically-thin  $\text{MoS}_2$ . For narrower diameters the high strain energy of  $\text{MoS}_2$  prohibited nanotube growth.<sup>10</sup> The unique excitonic, vibrational and conductive properties of each layer were disentangled for the composite (denoted  $\text{C@BN@MoS}_2$ ) by reference to the pristine CNT template and a radial heterostructure of CNTs wrapped only by BN (denoted  $\text{C@BN}$ ).

The composition and morphology of the 1D vdW heterostructures were directly imaged using scanning transmission electron microscopy (STEM). Low magnification annular dark-field (ADF) STEM images (Fig. 1a and 1b) and scanning electron microscopy images (Supplemental Fig. S1) demonstrated high purity, randomly oriented nanowires. Brighter regions in the dark-field STEM images result from areas with higher atomic number: hence the nanowires in Fig. 1a indicate predominantly the Mo atoms, while the nanowires in Fig. 1b show the extent of the BNNTs. These images directly attest to the high coverage of  $\text{MoS}_2$  NTs on the BNNT templates. Measurements on the CNT template film established the 2.1 nm diameter CNTs form bundles with mean diameter 7.9 nm. After BN overgrowth



the mean nanowire diameter was 11.1 nm (average 4-5 walls of BN), rising to 14.1 nm after MoS<sub>2</sub> growth (2-3 walls) [Supplemental Fig. S2].

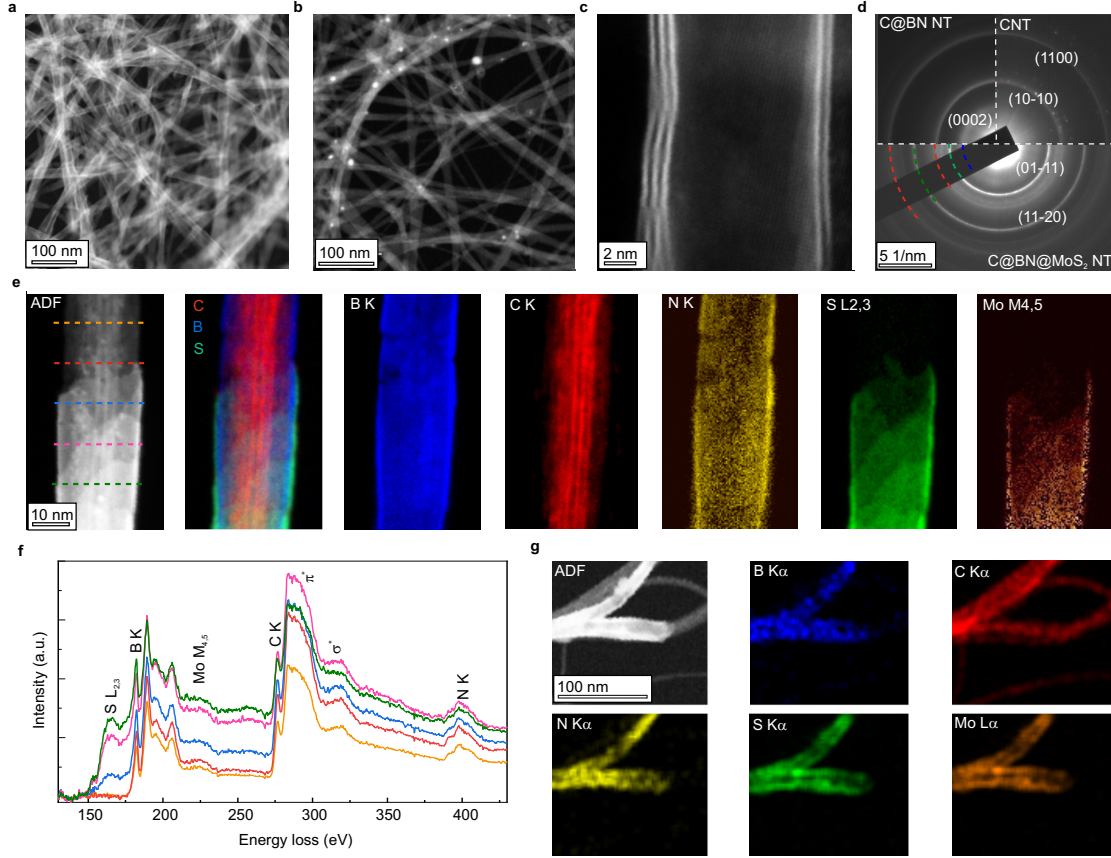


**Figure 1: Structure and composition of 1D vdW heterostructure.** ADF-STEM images of C@BN@MoS<sub>2</sub> NT (a) and C@BN NT (b) heterostructure films. (c) ADF image of multi-walled MoS<sub>2</sub> tube. (d) Selected-area electron diffraction obtained over a 3.5  $\mu\text{m}^2$  area for CNT (top-right), C@BN NT (top-left) and C@BN@MoS<sub>2</sub> NT (bottom) films. (e) ADF image of C@BN@MoS<sub>2</sub> NTs near the end of a MoS<sub>2</sub> NT, and the corresponding EELS elemental maps. From top to bottom an increase from zero to three MoS<sub>2</sub> walls can be observed, most clearly using the S L edge. (f) EELS spectra integrated along the five lines shown in (e); (g) ADF image of C@BN@MoS<sub>2</sub> NT heterostructure near the end of a MoS<sub>2</sub> NT, and the corresponding EDX elemental maps.

The typical wall thickness of the MoS<sub>2</sub> NTs was directly confirmed by ADF-STEM images: Fig. 1c shows a 1D vdW heterostructure with two MoS<sub>2</sub> walls (right) and three walls (left) indicating partial wrapping by a third MoS<sub>2</sub> nanotube. Selected-area electron diffraction patterns (Fig. 1d) showed diffraction rings consistent with randomly-oriented nanotubes

and the lattice constants of CNTs, multi-layer hexagonal BN (hBN) and MoS<sub>2</sub>. STEM electron energy loss spectroscopy (EELS near the end of an incomplete MoS<sub>2</sub> NT (Fig. 1e, f) and energy-dispersive X-ray spectroscopy (Fig. 1g) verified that the 1D heterostructure contained bundles of CNTs (red) covered by multi-walled BNNTs and MoS<sub>2</sub> NTs.

Each additional layer in a 1D vdW heterostructure may alter the optoelectronic properties of the final composite, either by detrimental changes to the encapsulated layers during overgrowth, or by interlayer charge or energy transfer. We assessed sample quality by comparing the equilibrium optical absorbance,  $A_0$ , for the pristine CNT film with that after each overgrowth. The C@BN@MoS<sub>2</sub> NT film exhibited an optical absorbance (Fig. 2a, green line) arising from the combination of the absorbance of atomically-thin crystalline MoS<sub>2</sub>, BN and C nanotubes, demonstrating that the growth process did not degrade the optoelectronic properties of the filling.

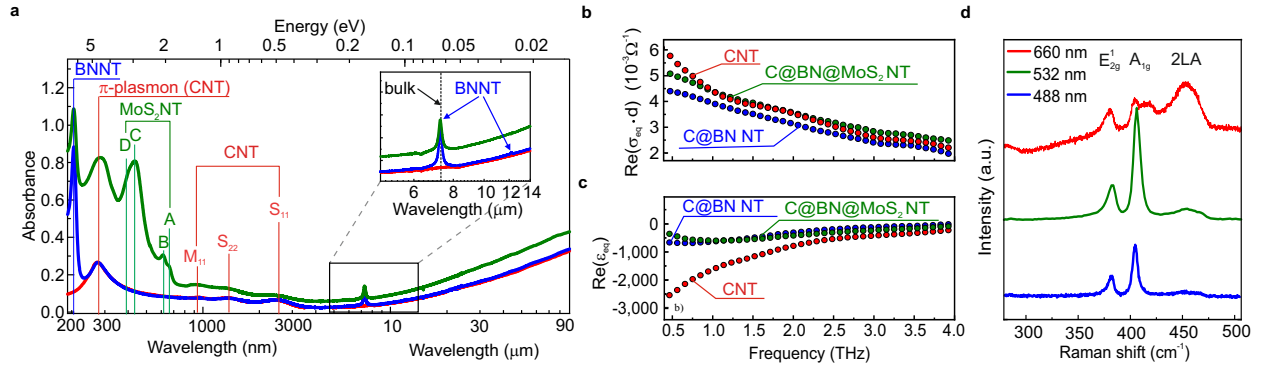


**Figure 2: Optical and vibrational properties of C, C@BN and C@BN@MoS<sub>2</sub> NTs.** (a) UV-visible-IR absorbance  $A_0 = 10^{-T}$  for C (red), C@BN (blue) and C@BN@MoS<sub>2</sub> (green) NT films. Near-infrared excitonic absorption peaks associated with semiconducting (S<sub>11</sub> and S<sub>22</sub>) and metallic (M<sub>11</sub>) SWCNTs are evident at 2300 nm, 1300 nm and 890 nm respectively. The sharp absorption at 205 nm (6.0 eV) is from the exciton in BN. The inset shows the in-plane stretch (1378 cm<sup>-1</sup>) and out-of-plane radial buckling (823 cm<sup>-1</sup>) modes associated with BN. The dashed black vertical line corresponds to the in-plane stretch mode of bulk h-BN (1367 cm<sup>-1</sup>).<sup>13</sup> (b) Real part of equilibrium conductivity of C (red empty circles), C@BN (blue empty circles) and C@BN@MoS<sub>2</sub> (green empty circles) NT films. (c) As (b), for the real part of the dielectric function in equilibrium. (d) Raman spectra of C@BN@MoS<sub>2</sub> NTs under 488 nm (blue), 532 nm (red) and 660 nm (green) laser excitation.

The absorption spectra of the C@BN@MoS<sub>2</sub> NTs show features associated with the ex-

citonic and interband absorption of MoS<sub>2</sub>, such as the A (660 nm, 1.88 eV) and B (613 nm, 2.02 eV) excitons, and the C (435 nm, 2.85 eV) and D (400 nm, 3.10 eV) interband transitions of MoS<sub>2</sub>,<sup>14,15</sup> similar to atomically-thin MoS<sub>2</sub>.<sup>16</sup> The A and B peaks in MoS<sub>2</sub> are associated with  $K$ -point excitons separated by the spin-orbit splitting energy of the valence band. For monolayer MoS<sub>2</sub> the conduction band (CB) minimum and valence band (VB) maximum coincide at the  $K$  point, with a single-particle direct bandgap of 2.1 eV.<sup>17</sup> For bilayer and thicker MoS<sub>2</sub>, the optical absorption at  $K$  is similar, but a rise in the valence band maximum at  $\Gamma$ , and a drop in the conduction band minimum at  $Q$ , creates an indirect gap material.<sup>5,17</sup>

Despite the strong absorption of the C@BN@MoS<sub>2</sub> film (around 4 times that of monolayer MoS<sub>2</sub><sup>18</sup>), no photoluminescence was observed for the 1D MoS<sub>2</sub> NTs, whereas under the same conditions a reference monolayer of 2D MoS<sub>2</sub> showed photoluminescence at the A exciton (Supplemental Fig. S3). This suggests that the MoS<sub>2</sub> nanotubes (2-3 monolayers) have an indirect bandgap, similar to bilayer and thicker 2D MoS<sub>2</sub>. Armchair, zigzag and chiral MoS<sub>2</sub> NTs were calculated to have similar optical absorption spectra,<sup>19</sup> particularly in the large diameter limit, with strong absorption above 2 eV similar to that observed here.

To elucidate intraband carrier motion in the 1D vdW heterostructures, the real parts of the effective THz conductivity,  $\text{Re}(\sigma_{\text{eq}})$  and the real parts of the effective dielectric function,  $\text{Re}(\epsilon_{\text{eq}})$ , are reported in Fig. 2(b) (see Fig. S4 for  $\text{Im}(\sigma_{\text{eq}})$ ). Here, the “effective” optical properties are averages over the composite, rather than representing local, microscopic response functions. The role of each layer is highlighted by the subtle changes evident between the reference C, C@BN and C@BN@MoS<sub>2</sub> NT films. The rise in  $\text{Re}(\sigma_{\text{eq}})$  towards lower frequency (higher wavelength) for the CNT film is consistent with previous studies of CNT films with a similar morphology, where the THz conductivity contains a contribution from Drude-like free-carrier absorption and from axial plasmons.<sup>20–22</sup> The C@BN NTs retain a large fraction of the conductivity of the CNTs ( $> 90\%$  at 1 THz), demonstrating that the inner CNTs in the heterostructure are highly conductive, and may be used to electrically gate the outer layers in future devices. The addition of the 4-5 insulating layers of BN reduces  $\text{Re}(\sigma_{\text{eq}})$  and

lowers the negative  $\text{Re}(\epsilon_{\text{eq}})$  characteristic of a highly conductive material. This suppression is most prominent at low frequencies, suggesting a lower dc conductivity. BN acts as a good tunnel barrier even for a monolayer,<sup>23</sup> and hence reduces intertube conductivity, while the intratube (plasmonic) conductivity remains comparable.

The addition of the MoS<sub>2</sub> NTs in the C@BN@MoS<sub>2</sub> composite creates a small increase in  $\text{Re}(\sigma_{\text{eq}})$  across the THz range in comparison to the C@BN NTs. This extra conductivity may be associated with free charges in the outer MoS<sub>2</sub>NT if the as-grown material is doped: indeed MoS<sub>2</sub> monolayers are often n-doped as a result of S-vacancies.<sup>24</sup> Alternatively, the MoS<sub>2</sub> NTs may have altered the conductivity of the encapsulated CNTs, either as a result of a strain-induced change in their bandstructure, or by a small but finite charge transfer from the outer MoS<sub>2</sub> NTs to the inner CNTs (possible given the estimated band alignment, Supplemental Fig. S5).

The C@BN and C@BN@MoS<sub>2</sub> NTs have distinct electronic and vibrational resonances that can be further investigated by Raman spectroscopy. The out-of-plane and in-plane Raman active phonons have been widely used to distinguish monolayer MoS<sub>2</sub> from bilayer and thicker structures, based on their position and splitting.<sup>25,26</sup> For the C@BN@MoS<sub>2</sub> NT film the in-plane  $E_{2g}^1$  and out-of-plane  $A_{1g}$  mode [Fig. 2 (d)], are in agreement with theoretical predictions for MoS<sub>2</sub> NTs.<sup>27,28</sup> Raman spectra taken for different laser wavelengths highlight the longitudinal acoustic (2LA) modes at 460 and 470 cm<sup>-1</sup>: these second-order Raman features are associated with intervalley electron transitions created by two LA phonons close to the  $K$  or  $M$  points, and which are relatively intense for resonant excitation of the A and B excitons,<sup>29</sup> as is evident here under excitation at 660 nm (resonant to the A exciton). A weak feature at  $\sim 420$  cm<sup>-1</sup> under 660 nm excitation is associated with a combination of LA and transverse acoustic (TA) phonon modes around the K point, due to a doubly-resonant intervalley electron scattering process.<sup>30</sup> The Raman results indicate that excitons in 1D MoS<sub>2</sub> nanotubes may undergo rapid intervalley charge transfer, as reported for 2D MoS<sub>2</sub>.<sup>30</sup>

To establish whether excitons in the MoS<sub>2</sub> nanotubes are the principle photoproduct

after light is absorbed by the MoS<sub>2</sub> component of the vdW heterostructure, we tracked the dynamical absorbance in the UV and visible range at different pump-probe delay times  $t$  after femtosecond pulsed excitation. In Fig. 3 broadband transient absorption spectra of the C@BN@MoS<sub>2</sub> NTs are shown for excitation at 350 nm (at energies above the D peak). The pump was absorbed predominantly in the MoS<sub>2</sub> NTs, which had high absorbance compared to the C and BN NTs (Fig. 2a) at this pump wavelength. The probe wavelengths (315-720 nm) covered the absorption range of the MoS<sub>2</sub> NTs, and were higher in energy than the  $S_{11}$ ,  $S_{22}$  and  $M_{11}$  energies where CNTs exhibit their transient response.<sup>31</sup>

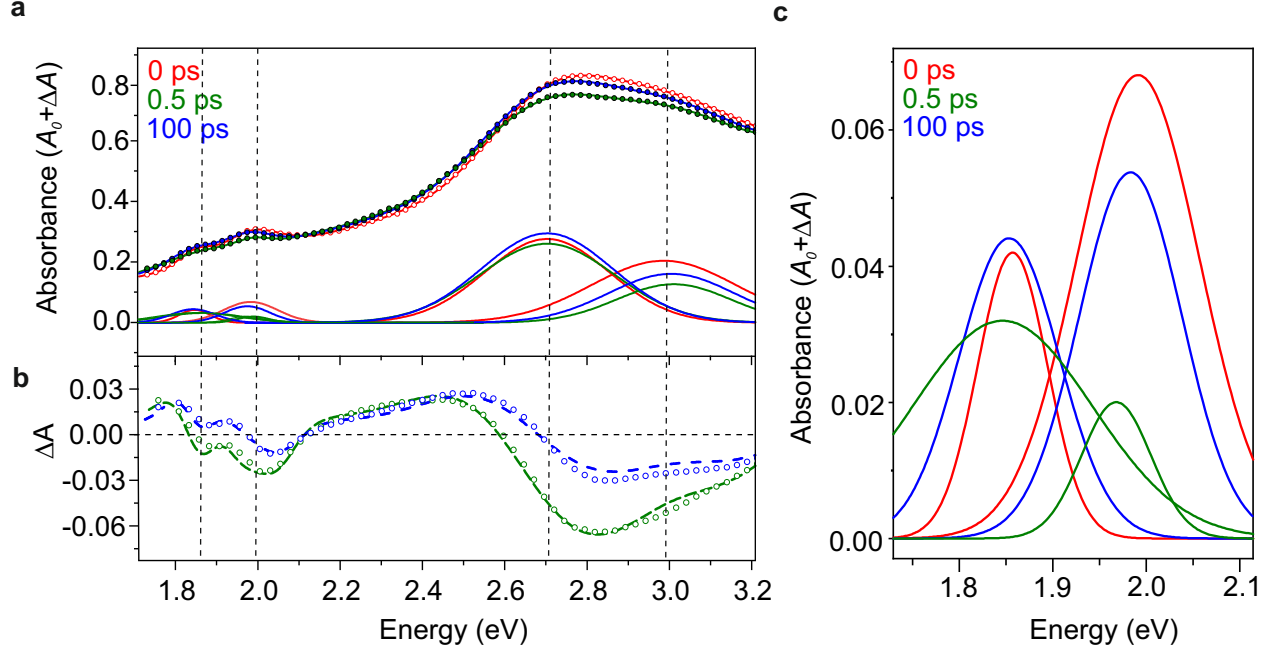


**Figure 3: Transient absorption spectroscopy of C@BN@MoS<sub>2</sub> NT film.** (a) Transient absorption spectra,  $A(E, t) = A_0(E) + \Delta A(E, t)$ , as a function of pump-probe delay time  $t$  and probe beam energy  $E$  (excitation wavelength 350 nm; 1 mJcm<sup>-2</sup> fluence). Here,  $t = 0.0$  ps was defined as the probe pulse arriving just before the pump pulse, and hence shows the equilibrium absorbance,  $A_0(E)$ , (empty red circles). Data at  $t = 0.5$  ps (green circles) and  $t = 100$  ps (blue circles) are also shown, along with fits (solid lines). The dashed vertical lines correspond (from left to right) to the A, B, C and D features in the equilibrium absorbance, while the contribution from each peak is shown by the lower colored lines. (b)  $\Delta A(E, t)$  spectra from experiment (circles) and corresponding fits (dashed lines) at  $t = 0.5$  ps (green) and  $t = 100$  ps (blue). (c) Expanded view of the fitted absorbance in the range near the A and B excitons, with the same color code as in (a).

The total absorbance spectra  $A(E, t) = A_0(E) + \Delta A(E, t)$  are reported in Fig. 3(a), where  $t = 0$  (red dashed line) corresponds to the probe arriving immediately prior to the pump, and thus shows the absorbance in equilibrium around the A, B, C and D peaks (dashed vertical lines). We modelled the experimental absorbance at each pump-probe delay using 4 resonances with variable energy, linewidth and strength (lower curves in Fig. 3(a)) superimposed on top of a monotonically increasing background accounting for the absorbance of the CNTs. The fitted  $\Delta A$  (Fig. 3(b), dashed lines) reproduced the experimental data (points). The contributions from the A and B excitons to the fitted absorbance is reported in Figure 3(c).

Prominent A and B excitonic absorption was present at all time delays, and at similar energies to equilibrium. From this we can conclude that, similar to the case of monolayer 2D MoS<sub>2</sub> and other TMDs, excitons are the primary photoproduct in the MoS<sub>2</sub> layers of the present vdW heterostructure. Further, the exciton dynamics are similar to those reported in monolayer MoS<sub>2</sub>,<sup>18</sup> suggesting that there was no substantial charge transfer to the CNT. Modifications to the strength and linewidth of the A and B excitons account for the observed  $\Delta A$  in the 1.7-2.2 eV range. Immediately after photoexcitation, the B exciton lowered in strength, but retained a similar linewidth to that in equilibrium [Figure 3(c)]. The A exciton broadened, and increased in strength above its equilibrium level after 1 ps, creating a positive  $\Delta A$  at energies below 1.98 eV (Supplemental Fig. S6). Similar trends were observed at all pump wavelengths, including resonant to the A exciton. Changes in the interband absorption strength (2.2-3.2 eV), including around the C and D peaks, were also evident, and can be linked to bandgap renormalization.<sup>18,32</sup>

The broader A-exciton linewidth results from faster energy, phase or momentum relaxation after photoexcitation, as in atomically-thin 2D TMDs.<sup>5</sup> However, the increase in A exciton strength here is unusual and may result from either the dynamic screening of the Coulomb interaction, or from trion formation. In the former case, the finite quasiparticle density screens the Coulomb interaction, lowering the binding energy and redshifting the

single-particle bandgap, with little change in the excitons' energies.<sup>5</sup> A weaker Coulomb interaction reduces the exciton oscillator strength, consistent with the B exciton's lower absorbance after photoexcitation, but inconsistent with the A exciton's increased strength. Alternatively, if the MoS<sub>2</sub> NTs are lightly doped in equilibrium (as suggested by the THz conductivity spectra above), the A exciton's absorption strength is partially reduced by Pauli blocking, similarly to the case for doped CNTs.<sup>22</sup> When the pump pulse injects excitons, the formation of trions removes the extrinsic charges from the conduction band or valence band, thereby removing the Pauli blocking effect and increasing the A exciton's absorbance, consistent with the experimental result.

To utilise 1D vdW heterostructures in nanoelectronic devices (e.g. photovoltaics) free charges may be desirable rather than excitons. Optical pump-THz probe (OPTP) spectroscopy allows the presence of free, unbound charges in semiconductor nanomaterials to be uniquely established.<sup>33,34</sup> While some studies of the THz photo-response of MoS<sub>2</sub> monolayers have reported positive photoconductivity linked to free carriers in an electron-hole plasma,<sup>35</sup> other studies reported negative photoconductivity assigned to trion formation,<sup>36</sup> in particular for n-doped monolayers.<sup>37</sup>

The dynamical THz photoconductivity of the 1D vdW heterostructures is reported in Figures 4 and 5. The magnitude and dynamic of the THz differential transmission  $\Delta T/T$  [Fig. 4(a)] was similar for the CNT and C@BN NT samples: as shown in Figure 2 BN did not absorb photons at the pump wavelengths used (340-950 nm), and BN encapsulation did not radically alter the optoelectronic properties of the CNTs. The C@BN@MoS<sub>2</sub> film exhibited a different dynamic [Fig. 4(a)], crossing from  $\Delta T/T > 0$  at early times to  $\Delta T/T < 0$  for  $t > 7$  ps. For pump wavelengths from 350 nm to 650 nm, corresponding to strong absorption of the pump in the MoS<sub>2</sub> NTs, this cross-over in  $\Delta T/T$  was universally observed [Fig. 4(b)]. However it was not seen at longer pump wavelengths (950 nm), when only the CNTs absorbed the pump.

This complex dynamic can be understood with reference to Figure 5. At early times, the

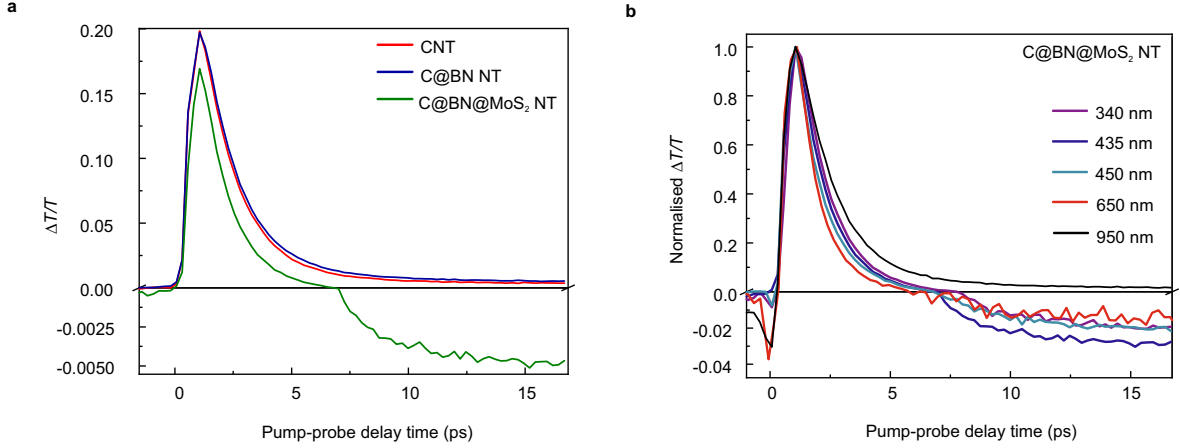


**Figure 4: Transient THz response of CNT, C@BN NT, C@BN@MoS<sub>2</sub> NT** (a) at 435 nm pump wavelength with  $100 \mu\text{Jcm}^{-2}$  fluence, (b) at 340 nm, 435 nm, 450 nm, 650 nm and 950 nm.

strong positive  $\Delta T/T$  for all samples can be attributed to optical excitation of the CNTs, which creates significant negative photoconductivity.<sup>22</sup> In equilibrium the CNTs are conductive, as a result of the metallic NTs and doped semiconducting NTs, with a conductivity similar to the Drude model of free-carrier absorption (black line, Fig. 5(a) inset). Optical excitation lowers the carrier density of free charges,  $n$ , or increases their effective masses,  $m^*$ .<sup>22</sup> A simultaneous narrowing of the conductivity spectrum results from a drop in the momentum scattering rate,  $\gamma$ ,<sup>22</sup> yielding a conductivity (blue line) lower than that in equilibrium, i.e. negative photoconductivity. At  $t = 2$  ps the real and imaginary parts of the experimental photoconductance [points, Fig. 5(b)] were modelled by the Drude function  $\Delta\sigma(\omega) = \sigma_D/(1 - i\omega\tau)$  [solid lines]. Here, the momentum scattering time was  $\tau = 1/\gamma = 110$  fs, while the dc photoconductance  $\sigma_D = -0.6$  mS (where  $1 \text{ mS} \equiv 10^{-3} \Omega^{-1}$ ) was negative to account for the lower conductivity under photoexcitation.

At later times the negative  $\Delta T/T$  corresponds to a positive photoconductivity uniquely associated with mobile charges in the MoS<sub>2</sub> NTs, and which persists for  $\sim 300$  ps (Supplemental Fig. S7). An excitonic origin can be ruled out: excitons in MoS<sub>2</sub> yield intraexcitonic transitions in the mid-infrared<sup>38</sup> instead of the THz.<sup>34</sup>



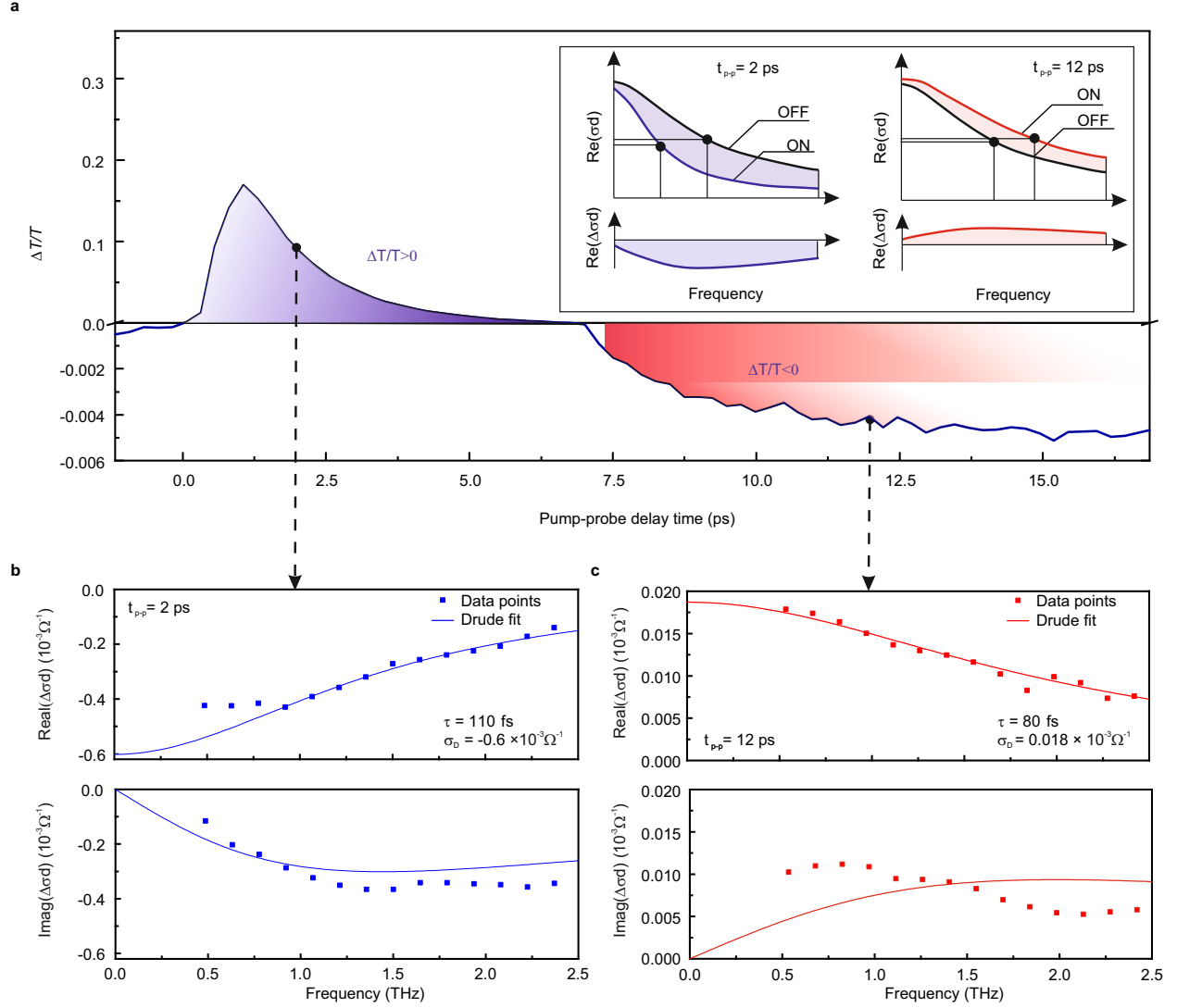


**Figure 5: Transient THz response of C@BN@MoS<sub>2</sub>** (a) versus pump-probe delay, at 435 nm pump wavelength and  $100 \mu\text{Jcm}^{-2}$  fluence. Note the negative and positive y-axes have different scales. The inset shows a schematic of the frequency-dependent conductivity without ('OFF') and with ('ON') photoexcitation, and their difference,  $\Delta\sigma(\omega)$ . (b) The real and imaginary parts of  $\Delta\sigma(\omega)$  at 2 ps (points) show a negative photoconductivity associated with the CNTs, which can be modelled by the Drude model (lines) as described in the text. (c) As in (b), but at 12 ps pump-probe delay, showing the positive photoresponse associated with normal photoconductivity in the MoS<sub>2</sub> NTs.

The real and imaginary parts of the experimental photoconductivity at  $t = 12$  ps [Fig. 5(d, e)] were modelled as at  $t = 2$  ps, but with a positive  $\sigma_D = 0.018$  mS and  $\tau = 80$  fs, corresponding to  $\gamma = 12.5$  THz. Assuming an effective mass  $m^* \simeq 0.6m_e$  representative of carriers in the K-valley of MoS<sub>2</sub>, the effective mobility of carriers in the MoS<sub>2</sub> NTs is  $\mu = e/m^*\gamma \simeq 234$  cm<sup>2</sup>/Vs. This is comparable to the best field-effect mobilities ( $\mu > 200$  cm<sup>2</sup>/Vs) obtained at room temperature in MoS<sub>2</sub> monolayers<sup>39</sup> and multilayered MoS<sub>2</sub>.<sup>40</sup> The THz mobility is a local probe of the intra-NT motion of free charges, and is higher than the mobility derived from transport measurements across multiple nanotubes, where charges cross multiple interfaces. Notably, the mobility observed here for MoS<sub>2</sub> NTs in a 1D vdW heterostructure is higher than the  $\sim 40$  cm<sup>2</sup>/Vs reported for individual multi-walled MoS<sub>2</sub> nanotubes,<sup>41</sup> and is also higher than reports for monolayer MoS<sub>2</sub> from OPTP spectroscopy.<sup>37,42</sup> Here, the relatively low momentum scattering rate and significant mobility attests to the high quality and relatively defect-free nature of the MoS<sub>2</sub> NTs.

The observation of free charges in the MoS<sub>2</sub> NTs is intriguing given the prominent excitons, although atomically-thin MoS<sub>2</sub> also exhibits both free charges and excitons.<sup>43,44</sup> Scenarios for the direct generation of free charges include exciton-exciton annihilation,<sup>43</sup> which is most effective at high exciton densities. Here the positive photoconductivity of the MoS<sub>2</sub> NTs was observed to increase linearly over a wide range of pump fluences (10-200  $\mu$ Jcm<sup>-2</sup>, Supplemental Fig. S8) suggesting that free charges are produced in proportion to the absorbed photon flux. At lower excitation densities, without exciton-exciton annihilation, exciton dissociation can proceed via electron trapping at defects,<sup>44</sup> leaving mobile holes. Further, the strong 2LA Raman modes resonant to the A-exciton (Figure 2) provide evidence that direct  $K$ -point excitons can be scattered into intervalley excitons<sup>5</sup> consisting of  $Q$ -point electrons and  $K$ -point holes.<sup>45</sup>

In conclusion, the structure of radial 1D van der Waals heterostructures consisting of carbon nanotubes wrapped by BN and MoS<sub>2</sub> nanotubes was studied on the atomic scale, while the effective optical properties of heterostructure films were examined from UV to

THz wavelengths. A dynamic switch from negative to positive photoconductivity originated from the differing temporal dynamics for free-carrier absorption in the carbon nanotubes and MoS<sub>2</sub> nanotubes. The conductivity of the carbon nanotube cores remained high after BN and MoS<sub>2</sub> fabrication, offering nano-scale electrical devices gated by the carbon nanotubes. Potential applications of these relatively large area ( $\sim 1\text{ cm}^2$ ) vdW heterostructure films include catalysis or gas sensing, where porous films are advantageous, or in optoelectronic devices requiring wafer-scale areas of high quality TMD semiconductor.

## Acknowledgements

The UK authors thank the EPSRC (UK) for support under grant EP/N010825/1. MGB thanks the Russian Government for financial support (Global Education program). This research received funding from projects 286546 (DEMEC), 292600 (SUPER) and 316572 (CNTstress) supported by the Academy of Finland, as well as projects 3303/31/2015 (CNT-PV) and 1882/31/2016 (FEDOC) supported by BF Finland.

## Competing interests

The authors declare no competing interests.

## Supporting information

Experimental methods (sample growth; spectroscopic methods) are described in the Supporting Information, which also includes additional electron microscopy and optical spectroscopy results as referenced from the main text. This material is available free of charge via the internet at <http://pubs.acs.org>.

## References

1. Mak, K. F.; Lee, C.; Hone, J.; Shan, J.; Heinz, T. F. Atomically Thin MoS<sub>2</sub>: A New Direct-Gap Semiconductor. *Phys. Rev. Lett.* **2010**, *105*, 136805.
2. Mak, K.; He, K.; Shan, J.; Heinz, T. Control of valley polarization in monolayer MoS<sub>2</sub> by optical helicity. *Nature Nanotechnology* **2012**, *7*, 494–498.
3. Ye, Z.; Cao, T.; O’Brien, K.; Zhu, H.; Yin, X.; Wang, Y.; Louie, S. G.; Zhang, X. Probing excitonic dark states in single-layer tungsten disulphide. *Nature* **2014**, *513*, 214 – 218.
4. Nagler, P.; Plechinger, G.; Ballottin, M. V.; Mitioglu, A.; Meier, S.; Paradiso, N.; Strunk, C.; Chernikov, A.; Christianen, P. C. M.; Schller, C. *et al.* Interlayer exciton dynamics in a dichalcogenide monolayer heterostructure. *2D Materials* **2017**, *4*, 025112.
5. Wang, G.; Chernikov, A.; Glazov, M. M.; Heinz, T. F.; Marie, X.; Amand, T.; Urbaszek, B. Colloquium: Excitons in atomically thin transition metal dichalcogenides. *Rev. Mod. Phys.* **2018**, *90*, 021001.
6. Park, S.; Mutz, N.; Schultz, T.; Blumstengel, S.; Han, A.; Aljarb, A.; Li, L.-J.; List-Kratochvil, E. J. W.; Amsalem, P.; Koch, N. Direct determination of monolayer MoS<sub>2</sub> and WSe<sub>2</sub> exciton binding energies on insulating and metallic substrates. *2D Materials* **2018**, *5*, 025003.
7. Zhang, J.-Z.; Ma, J.-Z. Two-dimensional excitons in monolayer transition metal dichalcogenides from radial equation and variational calculations. *Journal of Physics: Condensed Matter* **2019**, *31*, 105702.
8. Novoselov, K. S.; Mishchenko, A.; Carvalho, A.; Castro Neto, A. H. 2D materials and van der Waals heterostructures. *Science* **2016**, *353*.
9. Zollner, K.; Faria Junior, P. E.; Fabian, J. Proximity exchange effects in MoSe<sub>2</sub> and

- WSe<sub>2</sub> heterostructures with CrI<sub>3</sub>: Twist angle, layer, and gate dependence. *Phys. Rev. B* **2019**, *100*, 085128.
10. Xiang, R.; Inoue, T.; Zheng, Y.; Kumamoto, A.; Qian, Y.; Sato, Y.; Liu, M.; Gokhale, D.; Guo, J.; Hisama, K. *et al.* One-dimensional van der Waals heterostructures. *Science* **2020**, *367*, 537–542.
  11. Gong, L.; Wang, L.; Lu, J.; Han, C.; Chen, W.; Sow, C. H. Photocurrent Response in Multiwalled Carbon Nanotube CoreMolybdenum Disulfide Shell Heterostructures. *The Journal of Physical Chemistry C* **2015**, *119*, 24588–24596.
  12. Artyukhov, V. I.; Gupta, S.; Kutana, A.; Yakobson, B. I. Flexoelectricity and charge separation in carbon nanotubes. *Nano Letters* **2020**, acs.nanolett.9b05345.
  13. Lee, C. H.; Wang, J.; Kayatsha, V. K.; Huang, J. Y.; Yap, Y. K. Effective growth of boron nitride nanotubes by thermal chemical vapor deposition. *Nanotechnology* **2008**, *19*, 455605.
  14. Beal, A. R.; Knights, J. C.; Liang, W. Y. Transmission spectra of some transition metal dichalcogenides. I. Group IVA: Octahedral coordination. *Journal of Physics C: Solid State Physics* **1972**, *5*, 3531–3539.
  15. Aleithan, S. H.; Livshits, M. Y.; Khadka, S.; Rack, J. J.; Kordesch, M. E.; Stinaff, E. Broadband femtosecond transient absorption spectroscopy for a CVD MoS<sub>2</sub> monolayer. *Physical Review B* **2016**, *94*, 035445.
  16. Qiu, D. Y.; da Jornada, F. H.; Louie, S. G. Optical Spectrum of MoS<sub>2</sub>: Many-Body Effects and Diversity of Exciton States. *Phys. Rev. Lett.* **2013**, *111*, 216805.
  17. Nguyen, P. V.; Teutsch, N. C.; Wilson, N. R. N. P.; Kahn, J.; Xia, X.; Graham, A. J.; Kandyba, V.; Giampietri, A.; Barinov, A.; Constantinescu, G. C. *et al.* Visualizing

- electrostatic gating effects in two-dimensional heterostructures. *Nature* **2019**, *572*, 220–223.
18. Pogna, E. A. A.; Marsili, M.; De Fazio, D.; Dal Conte, S.; Manzoni, C.; Sangalli, D.; Yoon, D.; Lombardo, A.; Ferrari, A. C.; Marini, A. *et al.* Photo-induced bandgap renormalization governs the ultrafast response of single-layer MoS<sub>2</sub>. *ACS Nano* **2016**, *10*, 1182–1188.
  19. Milošević, I.; Nikolić, B. c. v.; Dobardžić, E.; Damnjanović, M.; Popov, I.; Seifert, G. Electronic properties and optical spectra of MoS<sub>2</sub> and WS<sub>2</sub> nanotubes. *Phys. Rev. B* **2007**, *76*, 233414.
  20. Zhang, Q.; Hároz, E. H.; Jin, Z.; Ren, L.; Wang, X.; Arvidson, R. S.; Lüttge, A.; Kono, J. Plasmonic nature of the terahertz conductivity peak in single-wall carbon nanotubes. *Nano Letters* **2013**, *13*, 5991–5996.
  21. Shao, D.; Yotprayoonsak, P.; Saunajoki, V.; Ahlskog, M.; Virtanen, J.; Kangas, V.; Volodin, A.; Haesendonck, C. V.; Burdanova, M.; Mosley, C. D. *et al.* Conduction properties of thin films from a water soluble carbon nanotube/hemicellulose complex. *Nanotechnology* **2018**, *29*, 145203.
  22. Burdanova, M. G.; Tsapenko, A. P.; Satco, D. A.; Kashtiban, R.; Mosley, C. D. W.; Monti, M.; Staniforth, M.; Sloan, J.; Gladush, Y. G.; Nasibulin, A. G. *et al.* Giant negative terahertz photoconductivity in controllably doped carbon nanotube networks. *ACS Photonics* **2019**, *6*, 1058–1066.
  23. Britnell, L.; Gorbachev, R. V.; Jalil, R.; Belle, B. D.; Schedin, F.; Katsnelson, M. I.; Eaves, L.; Morozov, S. V.; Mayorov, A. S.; Peres, N. M. R. *et al.* Electron tunneling through ultrathin boron nitride crystalline barriers. *Nano Letters* **2012**, *12*, 1707–1710.
  24. Shen, C.-C.; Hsu, Y.-T.; Li, L.-J.; Liu, H.-L. Charge dynamics and electronic structures

- of monolayer MoS<sub>2</sub> films grown by chemical vapor deposition. *Applied Physics Express* **2013**, *6*, 125801.
25. Lee, C.; Yan, H.; Brus, L. E.; Heinz, T. F.; Hone, J.; Ryu, S. Anomalous lattice vibrations of single- and few-Layer MoS<sub>2</sub>. *ACS Nano* **2010**, *4*, 2695–2700.
  26. Molina-Sánchez, A.; Wirtz, L. Phonons in single-layer and few-layer MoS<sub>2</sub> and WS<sub>2</sub>. *Phys. Rev. B* **2011**, *84*, 155413.
  27. Ghorbani-Asl, M.; Zibouche, N.; Wahiduzzaman, M.; Oliveira, A. F.; Kuc, A.; Heine, T. Electromechanics in MoS<sub>2</sub> and WS<sub>2</sub>: Nanotubes vs. monolayers. *Scientific Reports* **2013**, *3*, 2961.
  28. Evarestov, R. A.; Bandura, A. V. Infrared and Raman active vibrational modes in MoS<sub>2</sub>-based nanotubes: Symmetry analysis and first-principles calculations. *Journal of Computational Chemistry* **2018**, *39*, 2163–2172.
  29. Carvalho, B. R.; Wang, Y.; Mignuzzi, S.; Roy, D.; Terrones, M.; Fantini, C.; Crespi, V. H.; Malard, L. M.; Pimenta, M. A. Intervalley scattering by acoustic phonons in two-dimensional MoS<sub>2</sub> revealed by double-resonance Raman spectroscopy. *Nature Communications* **2017**, *8*, 14670.
  30. Gontijo, R. N.; Resende, G. C.; Fantini, C.; Carvalho, B. R. Double resonance Raman scattering process in 2D materials. *Journal of Materials Research* **2019**, *34*, 1976 – 1992.
  31. Gladush, Y.; Mkrtchyan, A. A.; Kopylova, D. S.; Ivanenko, A.; Nyushkov, B.; Kobtsev, S.; Kokhanovskiy, A.; Khagai, A.; Melkumov, M.; Burdanova, M. *et al.* Ionic liquid gated carbon nanotube saturable absorber for switchable pulse generation. *Nano Letters* **2019**, *9*, 5836–5843.
  32. Chernikov, A.; Ruppert, C.; Hill, H. M.; Rigosi, A. F.; Heinz, T. F. Population inversion

- and giant bandgap renormalization in atomically thin WS<sub>2</sub> layers. *Nature Photonics* **2015**, *9*, 466–470.
33. Ulbricht, R.; Hendry, E.; Shan, J.; Heinz, T. F.; Bonn, M. Carrier Dynamics in Semiconductors Studied With Time-Resolved Terahertz Spectroscopy. *Reviews of Modern Physics* **2011**, *83*, 543–586.
  34. Lloyd-Hughes, J.; Jeon, T. I. A Review of the Terahertz Conductivity of Bulk and Nanomaterials. *Journal of Infrared, Millimeter, and Terahertz Waves* **2012**, *33*, 871–925.
  35. Docherty, C. J.; Stranks, S. D.; Habisreutinger, S. N.; Joyce, H. J.; Herz, L. M.; Nicholas, R. J.; Johnston, M. B. An ultrafast carbon nanotube terahertz polarisation modulator. *Journal of Applied Physics* **2014**, *115*, 203108.
  36. Lui, C. H.; Frenzel, A. J.; Pilon, D. V.; Lee, Y.-H.; Ling, X.; Akselrod, G. M.; Kong, J.; Gedik, N. Trion-induced negative photoconductivity in monolayer MoS<sub>2</sub>. *Phys. Rev. Lett.* **2014**, *113*, 166801.
  37. Xing, X.; Zhao, L.; Zhang, Z.; Lin, X.; Yu, Y.; Jin, Z.; Liu, W.; Zhang, W.; Ma, G. The modulation of terahertz photoconductivity in CVD grown n-doped monolayer MoS<sub>2</sub> with gas adsorption. *Journal of Physics: Condensed Matter* **2019**, *31*, 245001.
  38. Cha, S.; Sung, J. H.; Sim, S.; Park, J.; Heo, H.; Jo, M.-H.; Choi, H. 1s-intraexcitonic dynamics in monolayer MoS<sub>2</sub> probed by ultrafast mid-infrared spectroscopy. *Nature Communications* **2016**, *7*, 10768.
  39. Radisavljevic, B.; Radenovic, A.; Brivio, J.; Giacometti, V.; Kis, A. Single-layer MoS<sub>2</sub> transistors. *Nature Nanotechnology* **2011**, *6*, 147–150.
  40. Strait, J. H.; Nene, P.; Rana, F. High intrinsic mobility and ultrafast carrier dynamics in multilayer metal-dichalcogenide MoS<sub>2</sub>. *Physical Review B* **2014**, *90*, 245402.



41. Fathipour, S.; Remskar, M.; Varlec, A.; Ajoy, A.; Yan, R.; Vishwanath, S.; Rouvimov, S.; Hwang, W. S.; Xing, H. G.; Jena, D. *et al.* Synthesized multiwall MoS<sub>2</sub> nanotube and nanoribbon field-effect transistors. *Applied Physics Letters* **2015**, *106*, 022114.
42. Docherty, C. J.; Parkinson, P.; Joyce, H. J.; Chiu, M.-H.; Chen, C.-H.; Lee, M.-Y.; Li, L.-J.; Herz, L. M.; Johnston, M. B. Ultrafast Transient Terahertz Conductivity of Monolayer MoS<sub>2</sub> and WSe<sub>2</sub> Grown by Chemical Vapor Deposition. *ACS Nano* **2014**, *8*, 11147–11153.
43. Sun, D.; Rao, Y.; Reider, G. A.; Chen, G.; You, Y.; Brzin, L.; Harutyunyan, A. R.; Heinz, T. F. Observation of rapid exciton - exciton annihilation in monolayer molybdenum disulfide. *Nano Letters* **2014**, *14*, 5625–5629.
44. Wang, H.; Zhang, C.; Rana, F. Ultrafast Dynamics of Defect-Assisted ElectronHole Recombination in Monolayer MoS<sub>2</sub>. *Nano Letters* **2015**, *15*, 339–345.
45. Selig, M.; Berghäuser, G.; Raja, A.; Nagler, P.; Schüller, C.; Heinz, T. F.; Korn, T.; Chernikov, A.; Malic, E.; Knorr, A. Excitonic linewidth and coherence lifetime in monolayer transition metal dichalcogenides. *Nature Communications* **2016**, *7*, 13279.

For table of contents only:

